BIRKHÄUSER

Deformation and Gravity Change: Indicators of **Isostasy, Tectonics, Volcanism,** and **Climate Change**

Edited by
Detlef Wolf
José Fernández

Birkhäuser
Basel · Boston · Berlin

Reprint from Pure and Applied Geophysics
(PAGEOPH), Volume 164 (2007) No. 4

Editors:

Detlef Wolf
Geoforschungszentrum Potsdam
Abteilung Geodäsie und Fernerkundung
Telegrafenberg
14473 Potsdam
Germany
dasca@gfz-potsdam.de

José Fernández
Instituto de Astronomía y
Geodesia (CSIC-UCM)
Spanish Council for Scientific Research
Fac. C. Matemáticas
Plaza de Ciencias, 3
28040 Madrid
Spain
jose_fernandez@mat.ucm.es

Library of Congress Control Number: 2007925494

Bibliographic information published by Die Deutsche Bibliothek:
Die Deutsche Bibliothek lists this publication in the Deutsche Nationalbibliografie; detailed bibliographic data is available in the Internet at <http://dnb.ddb.de>

ISBN 978-3-7643-8416-6 Birkhäuser Verlag AG, Basel · Boston · Berlin

Basel · Boston · Berlin
P.O. Box 133, CH-4010 Basel, Switzerland
Part of Springer Science+Business Media
Printed on acid-free paper produced from chlorine-free pulp. TCF ∞
Printed in Germany

ISBN 978-3-7643-8416-6
9 8 7 6 5 4 3 2 1

e-ISBN 978-3-7643-8417-3
www.birkhauser.ch

PURE AND APPLIED GEOPHYSICS
Vol. 164, No. 4, 2007

Contents

633 Deformation and Gravity Change: Indicators of Isostasy, Tectonics, Volcanism and Climate Change. Introduction
D. Wolf, J. Fernández

637 An Overview of the Small BAseline Subset Algorithm: A DInSAR Technique for Surface Deformation Analysis
R. Lanari, F. Casu, M. Manzo, G. Zeni, P. Berardino, M. Manunta, A. Pepe

663 Propagator-matrix Technique for the Viscoelastic Response of a Multi-layered Sphere to Surface Toroidal Traction
Z. Martinec

683 Using Fuzzy Logic for the Analysis of Sea-level Indicators with Respect to Glacial-isostatic Adjustment: An Application to the Richmond-Gulf Region, Hudson Bay
V. Klemann, D. Wolf

697 Shear-wave Velocity Structure around Teide Volcano: Results Using Microtremors with the SPAC Method and Implications for Interpretation of Geodetic Results
F. J. Chávez-García, F. Luzón, D. Raptakis, J. Fernández

721 Steric Sea-level Variations Inferred from Combined Topex/Poseidon Altimetry and GRACE Gravimetry
D. García, G. Ramillien, A. Lombard, A. Cazenave

733 Interpretation of 1992–1994 Gravity Changes around Mayon Volcano, Philippines, Using Point Sources
A. G. Camacho, J. Fernández, M. Charco, K. F. Tiampo, G. Jentzsch

751 Glacial-isostatic Adjustment and the Viscosity Structure Underlying the Vatnajökull Ice Cap, Iceland
K. Fleming, Z. Martinec, D. Wolf

769 Review of Microgravity Observations at Mt. Etna: A Powerful Tool to Monitor and Study Active Volcanoes
D. Carbone, F. Greco

791 An Estimate of Global Mean Sea-level Rise Inferred from Tide-gauge Measurements Using Glacial-isostatic Models Consistent with the Relative Sea-level Record
J. M. Hagedoorn, D. Wolf, Z. Martinec

819 Modeling of Stress Changes at Mayon Volcano, Philippines
K. F. Tiampo, J. Fernández, T. Hayes, G. Jentzsch

837 A Hybrid Model for the Summit Region of Merapi Volcano, Java, Indonesia, Derived from Gravity Changes and Deformation Measured between 2000 and 2002
C. Tiede, J. Fernández, C. Gerstenecker, K. F. Tiampo

851 Vertical Crustal Motion along the Mediterranean and Black Sea Coast Derived from Ocean Altimetry and Tide Gauge Data
D. García, I. Vigo, B. F. Chao, M. C. Martínez

865 Some Insights into Topographic, Elastic and Self-gravitation Interaction in Modelling Ground Deformation and Gravity Changes in Active Volcanic Areas
M. Charco, J. Fernández, F. Luzón, K. F. Tiampo, J. B. Rundle

Pure appl. geophys. 164 (2007) 633–635
0033–4553/07/040633–3
DOI 10.1007/s00024-007-0195-6

Pure and Applied Geophysics

Deformation and Gravity Change: Indicators of Isostasy, Tectonics, Volcanism and Climate Change. Introduction

Detlef Wolf[1,2] and José Fernández[3]

The workshop on *Deformation and Gravity Change: Indicators of Isostasy, Tectonics, Volcanism and Climate Change* took place at the Casa de los Volcanes on Lanzarote, Spain, during March 1–4, 2005 (see Fig. 1). It was jointly organized and supported by the International Association of Geodesy (IAG), the Spanish Ministry of Education and Science, the Spanish Council for Scientific Research and the Cabildo Insular de Lanzarote. From an organizational point of view, the workshop also served as the first meeting of the members the IAG Working Group ICCT2 on *Dynamic Theories of Deformation and Gravity Fields* existing since late 2003, but was open to all "external" colleagues interested in its topic.

Furthermore, it continued a tradition established by a series of preceding workshops organized under the auspices of the IAG and devoted to the themes "Models of Temporal Variations of the Gravity Field" (Walferdange, Luxembourg, March 17–19, 1997 and Potsdam, Germany, November 23–25, 1998) and "Dynamic Theories of Deformation and Gravity Fields" (Sopron, Hungary, February 19–23, 2001 and Lanzarote, Spain, February 18–21, 2003).

The common subject of these workshops reflects the major developments in geodynamics during the last decade, when temporal variations of the deformation and gravity fields recorded by the geodetic measuring techniques and reflecting isostatic, tectonic or volcanic processes in the Earth's interior as well as hydrologic or oceanographic processes on its surface have gained ever increasing importance. On the one hand, this development is the consequence of the introduction of novel and highly precise measuring techniques as a prerequisite for monitoring these variations.

[1] GeoForschungsZentrum Potsdam, Department 1, Geodesy and Remote Sensing, D-14473 Potsdam, Germany. E-mail: dasca@gfz-potsdam.de
[2] Geodetic Institute, University of Stuttgart, D-70174 Stuttgart, Germany.
[3] Instituto de Astronomía y Geodesia (CSIC-UCM), Fac. C. Matemáticas, Ciudad Universitaria, Plaza de Ciencias, 3, 28040 Madrid, Spain. E-mail: jose_fernandez@mat.ucm.es.

Figure 1
Some of the participants in the workshop *Deformation and Gravity Change: Indicators of Isostasy, Tectonics, Volcanism and Climate Change* before their visit of the Cueva de los Verdes on Lanzarote.

On the other hand, continuing improvements in the theoretical formulation of viscoelastic field theories and their numerical implementations are now reaching a level that allows us to model the various geodynamic processes in a more realistic way than has yet been possible and also to gain understanding of their intricate interference and coupling. The workshop held on Lanzarote during March 1–4 and the resulting articles collected in this special issue reflect this duality of the recent evolution: Whereas the preceding workshops had focussed on theoretical developments, equal weight has been given this time to the two aspects of our current understanding of geodynamics.

We would like to thank the Consejeria de Ciencia y Tecnología of the Cabildo Insular de Lanzarote, the Lanzarote Laboratory for Geodynamics (CSIC-UCM), the staff of the Casa de los Volcanes—in particular, its director Joaquin Naverán as well as Orlando Hernández and Jaime Arranz—and Cristina Bernal of the Timanfaya National Park administration for their support during the workshop.

Useful suggestions by Renata Dmowska during the preparation of this topical issue are appreciated. We thank all authors for their contributions and acknowledge the assistance of the following reviewers: F. Amelung, O. Bennike, A. Bonforte, C. Braitenberg, A. Braun, C. Gerstenecker, M. Ishii, E. Ivins, W. Jacoby,

T. Johnson, C. Kisslinger, V. Klemann, C.A. Locke, B. Lühr, P. Lundgren, J.J. Mallorqu, Z. Martinec, G. Milne, G.T. Mitchum, J. Morales, S. Okubo, M. Poland, G. Puglisi, G. Rodriguez-Velasco, F. Roth, H. Rymer, F. Sánchez-Sesma, E. Schrama, G. Spada, K.F. Tiampo, C. Tiede and B. Vermeersen.

Pure appl. geophys. 164 (2007) 637–661
0033–4553/07/040637–25
DOI 10.1007/s00024-007-0192-9

Pure and Applied Geophysics

An Overview of the Small BAseline Subset Algorithm: A DInSAR Technique for Surface Deformation Analysis

Riccardo Lanari,[1] Francesco Casu,[1,2] Mariarosaria Manzo,[1,3] Giovanni Zeni,[1,3] Paolo Berardino,[1] Michele Manunta,[2] and Antonio Pepe[4]

Abstract—We present an overview of the Differential SAR Interferometry algorithm referred to as Small BAseline Subset (SBAS) technique, that allows us to detect surface deformation and to analyze their space-time characteristics. Following the description of the main theoretical aspects of the algorithm, we present several results obtained by applying the SBAS approach in selected case studies relevant to phenomena affecting volcanic areas (Campi Flegrei caldera and Somma-Vesuvio complex, Italy), aquifers (Santa Clara area within the San Francisco bay, California) and landslides (Maratea Valley, Italy). The overall analysis is carried out by using multilook DInSAR interferograms with a spatial resolution of the order of 100×100 m, computed from SAR data acquired by the ERS-1 and ERS-2 sensors. In particular, we highlight the peculiarities of the SBAS technique and its surface deformation retrieval capability for what concerns both large-scale deformation phenomena and more localized displacement effects.

Key words: Differential SAR Interferometry, SBAS, surface deformation.

1. Introduction

Differential Synthetic Aperture Radar Interferometry (DInSAR) is a microwave remote sensing technique that allows us to investigate surface deformation phenomena with a centimeter to millimeter accuracy and with a large spatial coverage capacity (Gabriel *et al.*, 1989). In particular, the DInSAR technique exploits the phase difference, often referred to as interferogram, between two SAR images relevant to temporally separated observations of an investigated area and provides a measurement of the ground deformation projection along the radar line of sight (LOS).

[1] Istituto per il Rilevamento Elettromagnetico dell'Ambiente, National Research Council, via Diocleziano 328, 80124 Napoli, Italy.

[2] Dipartimento di Ingegneria Elettrica ed Elettronica, Università degli studi di Cagliari, Piazza d'Armi, 09123 Cagliari, Italy.

[3] Dipartimento di Ingegneria e Fisica dell'Ambiente, Università degli Studi della Basilicata, Viale dell'Ateneo Lucano 10, 85100 Potenza, Italy.

[4] Dipartimento di Ingegneria Elettronica e delle Telecomunicazioni, Università degli Studi di Napoli, Federico II, via Claudio 21, 80125 Napoli, Italy.

The DInSAR technology already plays an important role for surface displacement analysis and monitoring but we must remark that it also has key limitations, the most relevant being those due to the noise effects on the interferograms, referred to as decorrelation phenomena (ZEBKER and VILLASENOR, 1992). Intuitively, we can say that these noise phenomena are the consequence of any effect leading to differences in the "radar observation" of the imaged area, for what attains its electromagnetic response (reflectivity). The above mentioned differences may be caused by changes of the reflectivity of the zone which occurred between the two sensor passes (temporal decorrelation), or by the different imaging directions due to the spatial separation between the two acquisition orbits (spatial decorrelation). We further remark that the actual SAR scenarios mostly involve sensors operating at C-Band (5.3 GHz central frequency corresponding to a 5.6 cm wavelength) with a revisiting time of about 20–40 days and with a typical separation between the sensor orbits in the range of 0–2 km. Accordingly, we may expect low decorrelation effects mostly in urbanized and rocky areas while zones characterized by vegetation, agricultural fields, snow or water are drastically affected by noise (ROSEN *et al.*, 2000).

The DInSAR methodology has been applied first to investigate single deformation events (MASSONET *et al.*, 1993; PELTZER and ROSEN, 1995; RIGNOT, 1998). However, more recently, it also has been exploited to analyze the temporal evolution of the detected displacements via the generation of deformation time series. In this case, a time series of deformation can be solved for through the inversion of an appropriate sequence of DInSAR interferograms. The interest in the development of these methodologies is testified by several approaches which already have been presented or that are under development (FERRETTI *et al.*, 2000; BERARDINO *et al.*, 2002; MORA *et al.*, 2003; USAI, 2003; WERNER *et al.*, 2003; HOOPER *et al.*, 2004; CROSETTO *et al.*, 2005).

In this work we concentrate on the technique referred to as Small BAseline Subset (SBAS) approach proposed by BERARDINO *et al.* (2002), whose capability to detect and investigate deformation phenomena has been already shown in different applications, mostly based on exploiting the European Remote Sensing (ERS) SAR data, acquired in C-Band (LANARI *et al.*, 2002; LANARI *et al.*, 2004a; LANARI *et al.*, 2004b; LUNDGREN *et al.*, 2004; BORGIA *et al.*, 2005; MANZO *et al.*, 2006; CASCINI *et al.*, 2006). In particular, we focus on the basic SBAS technique that has been originally developed to investigate large spatial scale displacements with relatively low resolution (typically of the order of 100×100 m), by using low-pass filtered (multilook) DInSAR interferograms (ROSEN *et al.*, 2000). The key point of the SBAS technique, in addition to the previously mentioned use of multilook interferograms, is that the data pairs involved in the generation of the interferograms are properly selected in order to minimize the spatial and temporal separation (baseline) between the acquisition orbits, thus mitigating the decorrelation phenomena.

The SBAS procedure allows us to produce mean deformation velocity maps and, at the same time, deformation time series for each coherent pixel[1] of the investigated area. However, we also stress that the SBAS approach suffers some of the previously discussed limitations of the actual C-Band DInSAR technology. Indeed, despite the applied small (spatial and temporal) baseline constraints on the selected SAR data pairs, the density of the coherent pixels is typically not homogeneous in the scene and the technique can provide spatially dense results mostly in urban and rocky areas where the decorrelation phenomena have a very limited impact.

The key purpose of the work is to first provide a discussion of the SBAS algorithm basic theory and, more widely, to present results achieved by applying the approach to ERS SAR data, in selected case studies relevant to deformation phenomena affecting volcanic areas, aquifers and landslides.

For what concerns the volcano displacement analysis, we consider the Campi Flegrei caldera and the Vesuvio volcanic complex, both located in the Napoli Bay area (Italy). A second set of results is relevant to the San Francisco zone (California) with the analysis we present, focused on the Santa Clara aquifer. Finally, we investigate the gravitational phenomena affecting the Maratea Valley, which is located in southern Italy.

The overall analysis provides a quite large overview of the SBAS algorithm rationale and of its deformation retrieval capability in the various investigations.

2. Basic Theory of the SBAS Algorithm

The SBAS technique is a DInSAR approach allowing us to detect Earth's surface deformation and, above all, to analyze their temporal evolution. In particular, it relies on the use of a large number of SAR acquisitions and implements an easy combination of the multilook DInSAR interferograms computed from these data, finally leading to the generation of mean deformation velocity maps and time series. A detailed discussion on the SBAS approach is clearly outside the scope of this work and can be found in BERARDINO *et al.* (2002). Accordingly, we will present in the following the key points of the algorithm[2].

We start our discussion by providing first an intuitive explanation of the approach implemented by the SBAS procedure for retrieving the deformation signals. To achieve this task the algorithm first implements a selection of the coherent pixels in which the noise effects can be assumed negligible. On these pixels a decoupling of the deformation signal component from the undesired patterns,

[1] Note that we refer to coherent SAR pixels of the interferograms if they are characterized by a significantly high signal to noise ratio (SNR); thus, this implies low decorrelation effects.

[2] Note that we will maintain the same notation of BERARDINO *et al.* (2002).

referred to as topographic and atmospheric artifacts, is carried out by exploiting the characteristics of these patterns. In particular, the interferometric phase component relevant to the topographic artifacts is correlated with the vector of the spatial baselines (more specifically of the perpendicular baselines component with respect to the radar line of sight) of the interferograms sequence; moreover, the atmospheric phase signals are highly correlated in the space but poorly in time (FERRETTI *et al.*, 2000). Based on these characteristics, the SBAS procedure performs an estimation of these undesired signals that are subsequently filtered out from the measured interferometric phase, finally leading to the generation of the deformation time series.

We now provide more analytical details of the SBAS approach. Accordingly, we start by considering a set of $N + 1$ SAR images relative to the same area, acquired at the ordered times $(t_0, \ldots, t_N)$. We also assume, for sake of simplicity, that all the images are coregistered with respect to a single one (referred to as master) in order to have a common reference grid.

The starting point of the proposed technique is represented by the generation of a number, say M, of differential interferograms involving the previously mentioned set of $N + 1$ SAR acquisitions, properly generated in order to mitigate the decorrelation phenomena. To achieve this task, the SAR image pairs selected for the interferograms generation are characterized by a small spatial and temporal baseline as well as by a small frequency shift between the Doppler centroids (FRANCESCHETTI and LANARI, 1999). Note also that, as a consequence of these constraints, the SAR images involved in the interferograms generation could be grouped in several independent small baseline subsets that must be appropriately "linked" in order to retrieve the deformation time series.

We further remark that, since the phase information in the computed interferograms represents the modulo-2π restriction (wrapped) of the original (unwrapped) interferometric signal, each interferogram is processed in order to retrieve the original phase. This operation is referred to as phase unwrapping and is carried out, in our case, via a two-step approach. In particular, we first apply the minimum cost flow algorithm proposed by COSTANTINI and ROSEN (1999); the second step is represented by a region growing procedure allowing us to expand the unwrapped data in areas with lower coherence, i.e., lower SNR.

Let us now refer to a generic pixel of our SAR images with azimuth and range coordinates (x, r) and assume that the phase signal of each unwrapped interferogram is referenced to a pixel characterized by high coherence, whose deformation behavior is known *a priori* (typically, it is located in a non-deforming zone). Note that the selection of this reference SAR pixel must be carefully carried out because any error affecting this point will influence the overall results. In this context, particularly critical can be the impact of the atmospheric phase artifacts that, as already remarked, are spatially correlated, thus can be confused with deformation signals (BEAUDUCEL *et al.*, 2000).

The expression of the generic *j-th* interferogram computed from the SAR acquisitions at times t_B and t_A is, according to BERARDINO *et al.* (2002), the following:

$$\begin{aligned}\delta\phi_j(x,r) &= \phi(t_B,x,r) - \phi(t_A,x,r) \\ &\approx \frac{4\pi}{\lambda}[d(t_B,x,r)\text{–}d(t_A,x,r)] + \frac{4\pi}{\lambda}\frac{B_{\perp j}\,\Delta z}{r\sin\vartheta} + \frac{4\pi}{\lambda}[d_{atm}(t_B,x,r) - d_{atm}(t_A,x,r)] \\ &\quad + \Delta n_j,\ \forall j = 1,\ldots,M,\end{aligned} \tag{1}$$

wherein λ is the transmitted signal central wavelength, $\phi(t_B,x,r)$ and $\phi(t_A,x,r)$ represent the phases of the two images involved in the interferogram generation and $d(t_B,x,r)$ and $d(t_A,x,r)$ are the radar line of sight projections of the cumulative deformation at times t_B and t_A, with respect to the instant t_0 assumed as a reference, i.e., implying $\phi(t_0,x,r) = 0, \forall(x,r)$. Moreover, concerning the right-hand side in equation (1), the second term accounts for possible topographic artifacts Δz that can be present in the Digital Elevation Model (DEM) used for the interferograms generation; it depends on the perpendicular baseline component $B_{\perp j}$ (also referred to as spatial baseline) as well as on the sensor-target distance r and on the look angle ϑ. The terms $d_{atm}(t_A,x,r)$ and $d_{atm}(t_B,x,r)$ account for possible atmospheric phase artifacts (GOLDSTEIN, 1995) and the last term Δn_j for the decorrelation effects.

The expression (1) allows us to define a system of M equations in the N unknowns $\phi(t_i,x,r), \forall i = 1,\ldots,N$, which can be reorganized, by using a matrix formalism, as follows:

$$A\phi = \delta\phi, \tag{2}$$

wherein A is an incidence-like matrix directly related to the set of interferograms generated from the available data, see BERARDINO *et al.* (2002). Note also that the SBAS technique implies a pixel-by-pixel temporal analysis; accordingly, the dependence on the variables (x,r) has been neglected in (2) and this simplification will be maintained hereafter in the overall matrix representation.

We may now manipulate the system of equation (2) in such a way to replace the present unknowns with the mean phase velocity between time adjacent acquisitions. Accordingly, the new unknowns become:

$$v = \left[v_1 = \frac{\phi(t_1,x,r)}{t_1 - t_0}, \ldots, v_N = \frac{\phi(t_N,x,r) - \phi(t_{N-1},x,r)}{t_N - t_{N-1}}\right] \tag{3}$$

and, by substituting (3) in (2), we finally get the new system of equations:

$$Bv = \delta\phi, \tag{4}$$

wherein B represents an $M \times N$ matrix whose expression can be found in BERARDINO *et al.* (2002).

A few considerations of the system of equation (4) are in order. First of all, we remark that the previously mentioned (possible) separation of the SAR data into independent subsets causes a rank deficiency of the matrix B, leading the system (4) to have infinite solutions. However, the application of the Singular Value Decomposition (SVD) method, carried out within the SBAS procedure, allows us to evaluate the pseudo-inverse of the matrix B, which gives the minimum norm Least-Squares (LS) solution of the system (4). In this context, the mentioned minimum norm constraint for the velocity vector v allows us to mitigate the presence of large discontinuities in the final result, thus guaranteeing a physically sound solution as shown by LANARI *et al.* (2004c); this consideration is at the base of the data manipulation leading to (4). Obviously, an additional integration step is necessary to compute the solution ϕ from the estimated vector v, although this represents a trivial operation.

As a further remark we observe that, after resolving the system of equation (4), an estimation of the topographic artifacts Δz and of the atmospheric signal component $d_{atm}(.)$, see equation (1), is carried out. In particular, the evaluation of Δz benefits from the characteristics of the topographic phase component that is correlated with the perpendicular baseline vector $(B_{\perp_1}, \ldots, B_{\perp_M})$; note also that the need for the estimation of the topographic factor in equation (1) could appear irrelevant due to the hypothesis of small spatial baseline interferograms. However, since the amplitude of local topographic artifacts may significantly exceed the expected DEM accuracy, it can cause, if uncompensated, a remarkable quality degradation of the produced DInSAR fringes.

For that which concerns the mitigation of possible atmospheric phase artifacts, a filtering operation is performed that, as already highlighted, is based on the observation that the atmospheric signal component is highly correlated in space but poorly in time (FERRETTI *et al.*, 2000). Accordingly, the undesired atmospheric phase signals are estimated through the cascade of a low-pass filtering step in the two-dimensional spatial domain and a temporal high-pass filtering operation. Moreover, this procedure also allows us to detect possible orbital ramps caused by inaccuracies in the SAR sensors orbit information (LANARI *et al.*, 2004b). Finally, a filtering step is carried out in order to remove the detected atmospheric artifacts and orbital ramps.

In summary, the SBAS technique, whose block diagram is depicted in Figure 1, allows us to satify two key requirements:

— maximize the "temporal sampling rate" of the retrieved displacements signals by using nearly all the available SAR acquisitions;
— preserve the capability of the system to provide spatially dense deformation maps, which is a key feature of conventional DInSAR interferometry, by exploiting SAR data pairs with limited baseline values.

Accordingly, the SBAS approach permits us, by using standard multilook DInSAR interferograms, to detect and follow the temporal evolution of surface deformation with a high degree of temporal and spatial coverage.

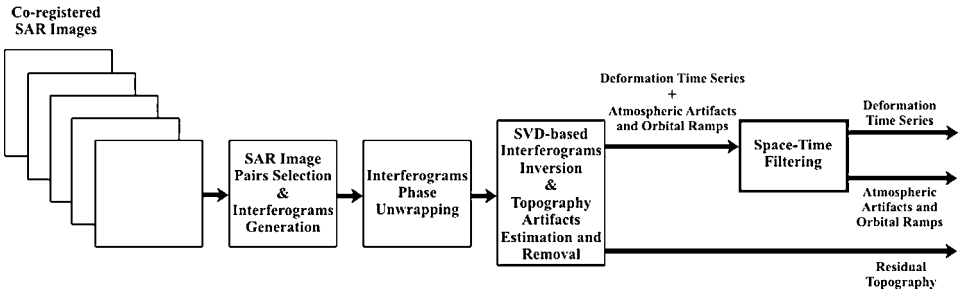

Figure 1
Block diagram of the SBAS algorithm.

3. SBAS-DInSAR Results

The following section presents a selection of results that have been recently achieved by applying the SBAS algorithm. In particular, we analyze the surface deformation effects relevant to different phenomena affecting volcanic areas, aquifers, and landslides. The overall set of results is based on processing data acquired by the ERS sensors (see Table 1 for a description of the sensors characteristics) and provides a clear idea of the surface deformation retrieval capability of the SBAS procedure.

3.1. Surface Deformation Analysis in Volcanic Areas: The Campi Flegrei and Vesuvio Case Study

3.1.1. Site description

The Neapolitan Volcanic area, localized in the southern sector of the Piana Campana, includes three active volcanoes: the Campi Flegrei caldera, Ischia Island

Table 1

Main characteristics of the ERS-1 and ERS-2 SAR sensors

Organization	European Space Agency (ESA)
Platform	Satellite
Launch Date	7/1991 (ERS-1), 4/1995 (ERS-2)
Frequency (GHz)	5.3 (C-band)
Polarization	VV
Orbit Altitude (km)	780
Orbit Inclination (deg)	98.5
Look Angle (deg)	23
Swath Width (km)	100
Antenna Dimensions (m)	10. × 1.
Pulse Duration (μS)	37.1
Pulse Bandwidth (MHz)	15.5
Pulse Repetition Frequency (Hz)	1640–1720
Transmitted Peak Power (kW)	4.8
Data Rate (Mbps)	105 (5 bits/sample, I/Q)

and the Somma-Vesuvio complex, that represent high sources of risk to the surrounding population. In the following analysis we focus on the portion of the Napoli Bay area that includes the two largest volcanoes of the zone, i.e., the Campi Flegrei caldera and the Somma-Vesuvio volcanic complex (see Fig. 2.).

Campi Flegrei caldera, located to the west of the City of Napoli within a densely populated urban area, is a volcanic field where numerous, different eruptive centers have been active over the past 39 ka. The beginning of volcanic activity of Campi Flegrei is not known precisely: sequences of lavas and pyroclasts approximately 2 million years in age have been found in several boreholes. However, the caldera is mainly the result of two principal collapse events related to the Campanian Ignimbrite eruption (39 ka) and to the Neapolitan Yellow Tuff eruption (15 ka), respectively, see ORSI *et al.* (1996) and DI VITO *et al.* (1999). Its evolution has been characterized by intense deformation phenomena (long and short-term deformation) with strong changes of the ground level. The Campi Flegrei magmatic system is still active and over the past 30 years the caldera has experienced episodes of rapid and large amplitude uplift with displacements of several meters. During the two bradyseismic crises of 1969–1972 and 1982–1984, the maxima ground uplifts were of about 170 cm and 180 cm, respectively, see

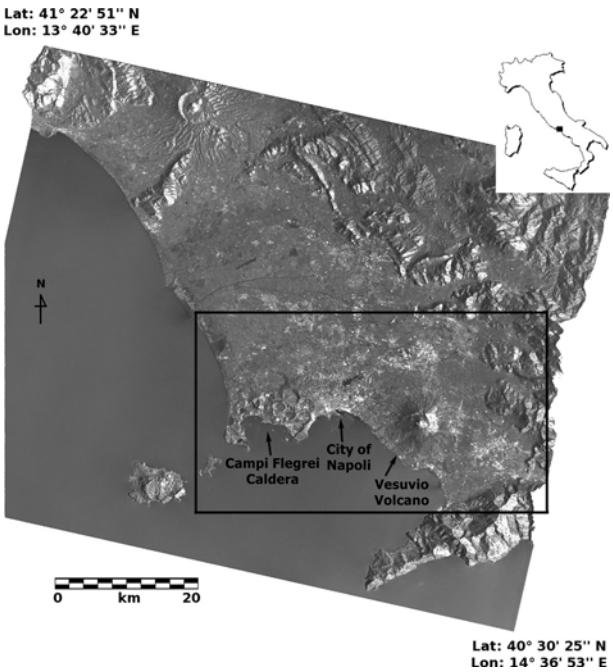

Figure 2
SAR image of the Campania Region (Italy). The black box identifies the investigated Napoli Bay area; the main sites of the zone have been also highlighted. The inset in the upper right corner shows the location of the area.

BIANCHI *et al.* (1987), DVORAK and GASPARINI (1991). These phenomena have been followed by longer term subsidence investigated also via DInSAR techniques (AVALLONE *et al.*, 1999; LUNDGREN *et al.*, 2001; BEAUDUCEL *et al.*, 2004); in particular, the results of the DInSAR data inversion presented by LUNDGREN *et al.* (2001) support the interpretation of subsidence due to hydrothermal diffusion as the main deformation mechanism during this phase of caldera deflation. We further remark that the caldera long-term subsidence phenomenon has been interrupted during 2000 by an uplift event whose deformation also has been analyzed by jointly applying SAR and classical geodetic techniques (LANARI *et al.*, 2004a); after 2000 a restart of the deflation has been recorded.

The Somma-Vesuvio volcano complex (maximum height 1281 m above sea level), located to the southeast of the City of Napoli, is one of the best known volcanoes in the world due to the historic Plinian eruption of 79 A.D. The volcanic activity in the area began at least 400 ka ago, as testified by lavas found (in boreholes) at 1350 m depth, while the history of the Somma-Vesuvio volcanic edifice began almost 25 ka ago with the growth of Mt. Somma. The first Plinian eruption of Pomici di Base (18.3 ka ago) marked the beginning of severe change in the shape of the Somma volcanic edifice, with the formation of a caldera due to the collapse of its summit. The next activity contributed to the growth of the more recent Vesuvio volcano inside this caldera. Its activity has been characterized by great variability both in styles of eruptions and in chemical composition of the emitted magmas. Since the last eruption in 1944, the volcano is in a quiescent stage, its activity limited to the occurrence of local seismicity consisting of some hundreds of events per year reaching maximum magnitudes of 3.7 (DE NATALE *et al.*, 2004). We further remark that deformation phenomena of the Somma-Vesuvio complex have been detected via DInSAR techniques (LANARI *et al.*, 2002) and an interpretation of these effects in terms of volcanic spreading has been recently given (BORGIA *et al.*, 2005).

3.1.2. Results

In order to exploit the capability of the SBAS approach to investigate the deformation of the Campi Flegrei caldera and of the Vesuvio volcano we have processed 116 SAR data acquired by the European Space Agency (ESA) ERS-1/2 sensors on both ascending (track 129, frame 809) and descending (track 36, frame 2781) passes. In particular, starting from the available SAR data set, we have computed 133 interferograms from 58 ERS acquisitions relevant to the ascending orbits spanning the January 1993 to May 2003 time interval. Moreover, 148 interferograms have been produced from 58 ERS acquisitions from descending orbits, collected between June 1992 and October 2002. Each interferometric SAR image pair has been chosen with a perpendicular baseline value smaller than 300 m and with a maximum time interval of 4 years; precise satellite orbital information and a DEM relevant to the Shuttle Radar Topography Mission (SRTM) (ROSEN *et al.*, 2001) have also been used. Moreover, all the DInSAR products have been obtained

following a complex multilook operation (ROSEN *et al.*, 2000) with four looks in the range direction and twenty looks in the azimuth one, with a resulting pixel dimension of about 100 × 100 m. Note also that the investigated SAR data set is the same exploited by BORGIA *et al.* (2005) for studying the Vesuvio volcano although in this case the processed area extends to the entire Napoli Bay zone.

A first result relevant to this area is presented in Figure 3, where the mean deformation velocity maps, computed (in SAR coordinates) from the ascending and the descending orbits data set, are shown. It is interesting to note the differences between the two geometries that allow also to understand how the radar sensor is imaging the investigated area.

The availability, in this study, of both ascending and descending data allows us to estimate, in addition to the conventional LOS displacements, also the east-west and vertical deformation components. Indeed, we can achieve this result by combining, equivalently to that shown by LUNDGREN *et al.* (2004), BORGIA *et al.* (2005) and MANZO *et al.* (2006), the mean displacement velocity maps computed from the ascending and descending orbits on pixels that are coherent in both maps (67% and 75% of the coherent pixels of the ascending and descending passes, respectively, for a total amount of about 56,000 points). In particular, the difference between these two patterns effectively eliminates their vertical and north velocity components and allows us to obtain an estimate of the surface deformation velocities in the east-west direction (see Fig. 4a). In contrast, the sum of the ascending and descending deformation patterns allows us to get a picture that is mostly vertical motion (see Fig. 4b). They have been computed with respect to a reference pixel that is located in the Napoli Harbor zone (black squares in Fig. 4), in correspondence to the reference

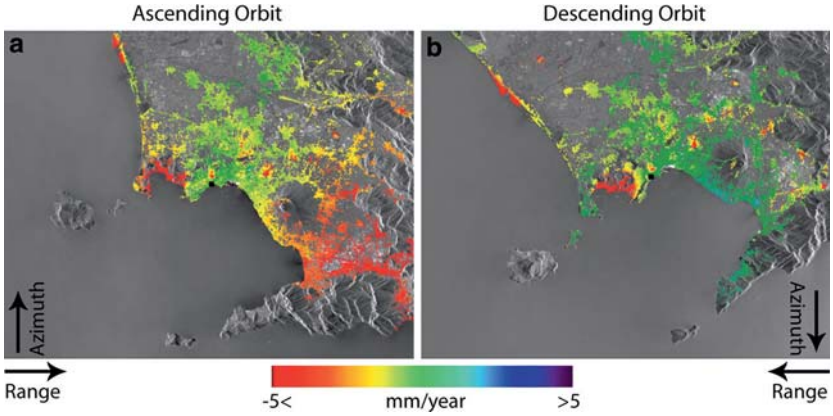

Figure 3
LOS mean deformation velocity maps of the Campania Region, represented in radar geometry, computed in coherent zones and superimposed to the SAR amplitude images: a) ascending orbit; b) descending orbit. Note that the red color corresponds to a sensor-target range increase; the azimuth and range directions are also highlighted. The black squares indicate the homologous reference pixels for the SAR measurements.

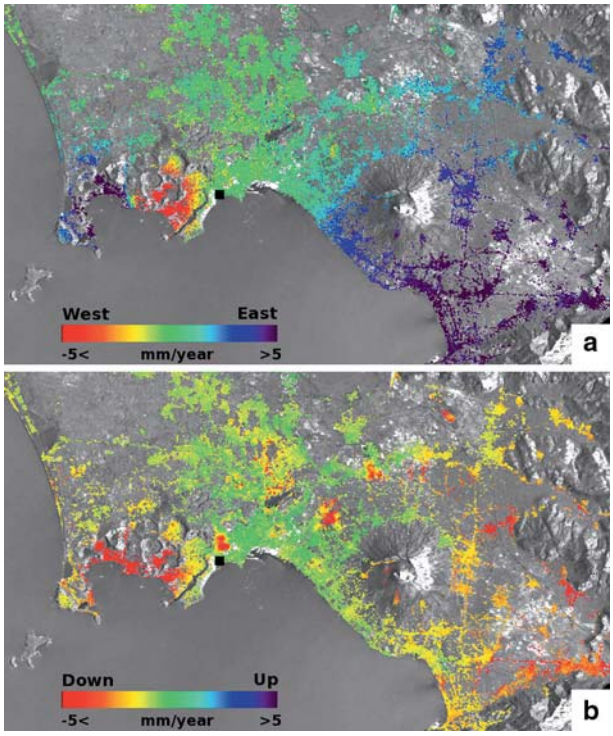

Figure 4
Mean deformation velocity maps relevant to the area highlighted by the black box in Figure 2, computed in coherent areas and superimposed to the SAR amplitude image: a) east-west component of the mean deformation velocity generated from the ascending and descending velocity patterns for pixels which are coherent in both maps; b) vertical component of the mean deformation velocity. Note that the red color corresponds in a) to a displacement toward west, in b) to a subsidence effect. The reference pixel for the SAR measurements, marked by a black square, is located in correspondence of the leveling benchmark referred to as LNA001, see (INGV-OV, 2001; 2002; 2003).

leveling benchmark LNA001. Note also that the DInSAR products shown in Figures 4a and 4b have been geocoded and superimposed on a SAR amplitude image of the zone; moreover, the noisy areas (non-coherent zones) with low accuracy measurements have been excluded.

By considering Figures 4a and 4b we note that reliable information is only available for the urbanized zones and rocky areas. This is particularly critical in the Vesuvio case where only a small part of the volcanic complex can be investigated due to extended vegetated zones. On the contrary, the highly urbanized characteristics of the Campi Flegrei caldera lead to a highly coherent site. Based on the results shown in Figures 4a and 4b, it is evident that the approach can provide information on the mean surface velocity displacements with a rather large spatial coverage. More specifically, by considering Figure 4a, two effects appear evident: the first corresponds to the peculiar deformation pattern of the Campi Flegrei caldera, related to

the long-term deflation, with the eastern and western sectors moving to the west and east, respectively; note also that the central area of the caldera, located in the Pozzuoli Harbor, is characterized by nearly no horizontal displacement. The second effect is related to a regional trend, showing the SE sector moving to the E relatively to the NW sector, as originally shown by BORGIA *et al.* (2005); in this case the transition between W and E displacements corresponds to an active regional tectonic structure previously highlighted by MAINO *et al.* (1963).

Regarding the vertical displacement signals shown in Figure 4b, we remark that also in this case several effects are visible. The first is a rather large displacement pattern relative to the Campi Flegrei caldera that is a peculiar feature relevant to the long-term subsidence. Other effects are several deformations found within the Napoli urban area (the largest one located in the Vomero Quarter, see TESAURO *et al.*, 2000; LANARI *et al.*, 2004d) and the occurrence of displacements on the summit of the Vesuvio volcano and in a sort of semi-corona located at the NW, N, NE, E, and SE base of the volcanic complex; these latter effects relevant to the Vesuvio volcano have been recently interpreted by BORGIA *et al.* (2005) in terms of a volcanic spreading phenomenon. Finally, the last detected effect corresponds to the regional subsidence of the eastern and southeastern sectors of the image.

We remark that the availability of the estimated vertical deformation component shown in Figure 4b is not only important for the analysis of the detected phenomena but also allows us to investigate the quality of the achieved DInSAR results. Indeed, in this case we may benefit from the presence in the Napoli Bay zone of one of the more extended leveling networks of the world with about 600 benchmarks and more than 350 km linear extension (INGV-OV, 2001, 2002, 2003). This geometric leveling network, that is managed by the Osservatorio Vesuviano (OV) belonging to the Italian National Institute of Geophysics and Volcanology (INGV), is a key element of the surveillance system of this area; indeed, it allows the achievement of high accuracy vertical measurements of deformation (mean square deviation of 0.1–0.2 mm/km are typical). Accordingly, we have compared the estimated vertical displacements available from the DInSAR measurements with the corresponding ones computed from the leveling data that are assumed as a reference. In particular, our comparison is focused on the leveling benchmarks identified by the squares shown in Figure 5a; note that this selection of benchmarks, which represents only a portion of the entire network, has been chosen because it permits us to ''connect'' the central deforming zones of the two investigated volcanoes. Moreover, the related leveling measurements, provided to us by OV-INGV, span the 1990–2003 time interval thus ensuring the temporal overlap with the available SAR data.

The achieved results of the DInSAR/leveling mean deformation velocity comparison are presented in the plot of Figure 5b. It clearly shows the good agreement between the two mean velocity measures (leveling: black stars, SAR: red triangles). Moreover, it also allows us to provide some interesting numbers relevant to the DInSAR products accuracy. To achieve this task, we have computed the

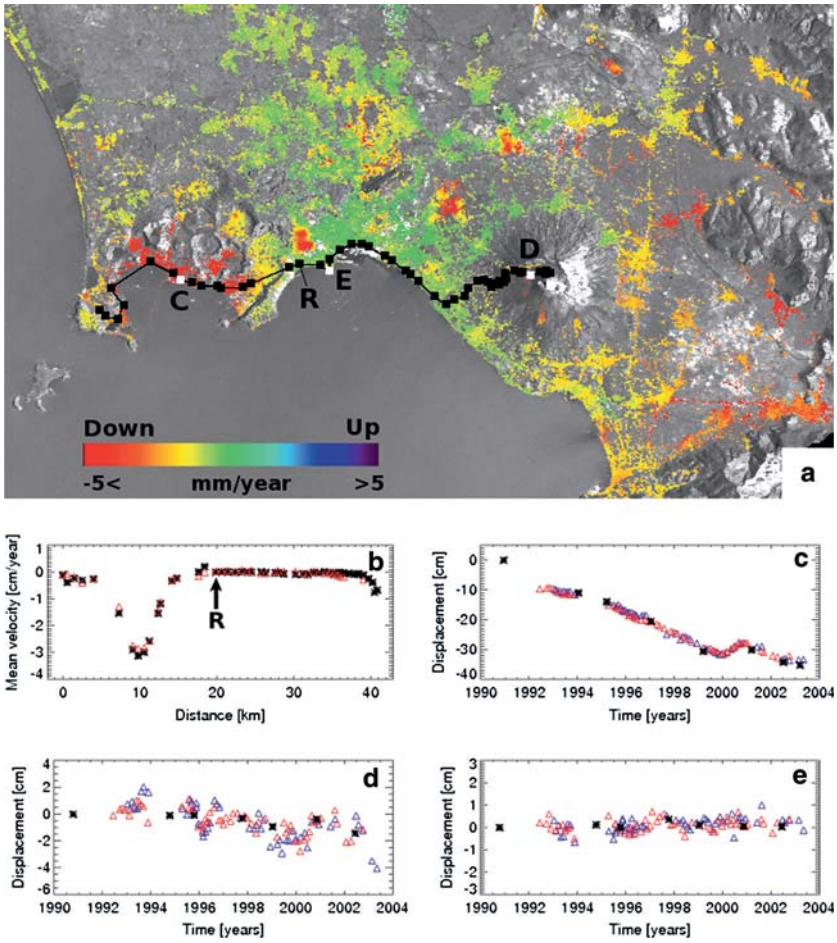

Figure 5

DInSAR/leveling comparison: a) vertical component of the mean deformation velocity (see Fig. 4b) superimposed with a selection of leveling benchmarks (black and white squares). The location of the reference benchmark LNA001, coincident with the reference SAR pixel, is identified by R; b) plot of the mean vertical deformation velocity computed from SAR data (red triangles) and from leveling data (black stars) corresponding with the benchmarks identified in Figure 5a; c–e) comparison between the DInSAR LOS deformation time series (ERS ascending data: blue triangles, ERS descending data: red triangles) and the leveling measurements (black stars) projected on the radar line of sight for the three pixels marked by white squares and labeled C, D and E in Figure 5a, respectively.

standard deviation value of the DInSAR/leveling difference that is equal to 0.11 cm/year. This result is consistent with those obtained through extended studies on the SBAS algorithm performance presented by Casu *et al.* (2005, 2006).

We further remark that the SBAS technique allows us to generate, in addition to the mean deformation velocity patterns, also deformation time series for each coherent pixel. This is a crucial information if we want to study the temporal

evolution of the displacements. To analyze this capability of the procedure, we have investigated the time series achieved from the SAR data relevant to the ascending and descending orbits. Moreover, in order to also compare in this case the DInSAR results with those available from the leveling measurements (the latter projected in the radar LOS with 23° mean look angle to allow the comparison with the ascending and descending DInSAR data), we focused our analysis on areas characterized by nearly vertical deformation only. Accordingly, we have identified first, from the result shown in Figure 4a, a selection of benchmarks with horizontal velocity amplitude below 0.25 cm/year and characterized by different deformation features in their time series; they are represented by the three white squares in Figure 5a and are labeled C, D and E (corresponding to the leveling benchmarks LCF/25A, LVE010 and LVE64B/18), respectively. For each of these benchmarks we have superimposed the line of sight projected leveling measurements (available in the SAR observation time window) and the deformation time series computed from the ascending and descending data, see Figures 5c, 5d and 5e, respectively. By observing the different plots shown in Figures 5c–5e, a strong similarity is clear between the temporal evolution of the ascending (blue triangles) and descending (red triangles) measurements as well as their agreement with the LOS projected leveling (black stars) deformation time series; the capability to follow the temporal evolution of the detected displacements via the SBAS retrieved time series is evident. In particular, by considering Figure 5c the presence is clear of a rather continuous subsidence phenomenon of the Campi Flegrei from 1992 until the beginning of 2000, when a change of the deformation trend occurred resulting in an uplift phase. For what concerns Figure 5d, it shows that the subsidence effect of the Vesuvio summit is rather continuous during the overall investigated time period. Finally, Figure 5e is relevant to a benchmark located in a non-deforming zone which represents a sort of control case in our set of experiments. Similar to what was done before we have computed, for all the benchmarks of Figure 5a, the difference between the DInSAR time series and the leveling data, the latter interpolated via a linear regression within the interval common to SAR data. The average values of the standard deviation of the computed differences amount to 0.44 cm for the ascending data and 0.47 cm for the descending ones, respectively. This is again consistent with what is expected from CASU *et al.* (2005, 2006).

3.2. Surface Deformation Analysis in Aquifer Areas: The Santa Clara Case Study

3.2.1. Site description

The Santa Clara valley aquifer is located within the San Francisco Bay area (California) (see Fig. 6), and represents a complex network of permeable, water-bearing units that exchange groundwater under different confining pressures. This area has experienced a long history of subsidence caused by an excessive pumping of groundwater (USGS Ground Water Atlas). In particular, starting from the

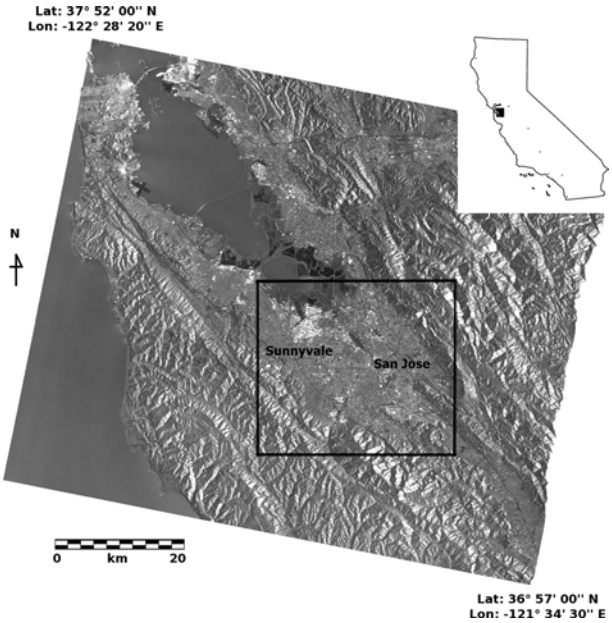

Figure 6
SAR image of the San Francisco area (California); the black box identifies the investigated zone relevant to the Santa Clara basin whose main sites have been also highlighted. The inset in the upper right corner shows the location of the area.

beginning of the twentieth century, extensive use of the groundwater resources has been carried out for agriculture purposes first, and then for urban and industrial developments. A decrease in rainfall during the first half of the twentieth century, coupled with an increase in the pumpage rate, finally led to subsidence phenomena reaching 5 m deformation (POLAND and IRELAND, 1988). Only in the mid-1960s effective actions for mitigating this subsidence were carried out; in particular, the importation of outside sources of water through the construction of various aqueducts represented a key element to offset the effects of groundwater withdrawal (USGS Ground Water Atlas). Moreover, also some percolation ponds were constructed on the valley margins in order to increase the recharge from winter runoff (SCHMIDT and BÜRGMANN, 2003). As a result of these actions, it was recorded through the late 1980s only a small amount of residual aquifer system compaction and subsidence (POLAND and IRELAND, 1988). Since then, no significant inelastic compaction (permanent subsidence) has been detected, while elastic displacements have been measured in response to seasonal variations in groundwater levels that also have been investigated via DInSAR techniques (GALLOWAY *et al.*, 2000; SCHMIDT and BÜRGMANN, 2003).

3.2.2. Results

We have applied the SBAS algorithm to a data set of 45 SAR images acquired on descending orbits by the ERS satellites, from mid 1992 to the end of 2000 (track 70, frame 2853), paired in 109 interferograms with a perpendicular baseline always smaller than 300 m and a maximum time interval of 4 years; precise satellite orbital information and an SRTM DEM of the study area have also been used. Moreover, all the interferograms have been obtained following a complex multilook operation, with four looks in the range direction and twenty looks in the azimuth one, with a resulting pixel dimension of about 100×100 m. These processing parameters are consistent with those applied for the generation of the DInSAR products relevant to the previous analysis of the volcanoes located in the Napoli Bay area (see section 3.1.2).

In order to provide an overall picture of the detected displacements, we present in Figure 7a the estimated LOS mean deformation velocity map that has been geocoded and superimposed on the SAR amplitude image of the investigated zone. By considering Figure 7a, two main uplift features appear in correspondence to the Sunnyvale zone (see Fig. 6) and of the area to the east of the Silver Creek fault highlighted in Figure 7a by a black line. The former has a maximum uplift velocity of 0.6 cm/year, while the latter of 0.4 cm/year. The deformation time series of two pixels selected (identified in Figure 7a by the white squares labeled E and F, respectively) are presented in the plots of Figures 7e and 7f, respectively. They clearly show a rather continuous trend that is related to artificial and/or natural recharge phenomena. However, the availability for each coherent pixel of Figure 7a of a deformation time series allows us to further expand our analysis, similar to that done by LANARI *et al.* (2004b) for the Santa Ana basin in southern California. Indeed, in order to investigate the seasonal oscillations of the Santa Clara basin, we have computed the correlation coefficient of each pixel's detrended time series, with a sinusoid within ± 60 days of March 10 in ten-day time bins. As a result of this analysis, we found a significant correlation with an annual oscillation (see Fig. 7b). Moreover, we have also computed the best-fitting sinusoid amplitudes (Fig. 7c) and the maximum correlation time centered on March 10 (Fig. 7d), in areas with correlation greater than 0.6. We found an interesting set of patterns: first of all, we noticed that the areas where deformation is highly correlated with the seasonal variations (see the two sample plots in Figs. 7g and

Figure 7 ▶

DInSAR results relevant to the investigated Santa Clara basin: a) LOS mean deformation velocity map computed in coherent areas and superimposed to the SAR amplitude image. The location of the Silver Creek fault (continuous and dashed black lines), of the reference SAR pixel labeled R and of the sample pixels labeled E, F, G, and H, also have been highlighted; b) maximum correlation map between the SAR time series and an annual sinusoid (falling within $\pm$ 60 days of March 10); c) peak to peak amplitude of the sinusoid computed in the area where the correlation map shown in Figure 7b is greater than 0.6; d) time shift of the sinusoid relative to the center date of March 10; e-h) deformation time series relevant to the pixels labeled E, F, G and H in Figure 7a, respectively. Note that in Figures 7g and 7h the trended sinusoid (black line) corresponding to the maximum correlation also has been plotted.

7h) are sharply bounded by the northward extension of the Silver Creek fault, which is clearly detectable in Figure 7b. This result is consistent with the interpretation of the fault as a hydrological barrier to groundwater flow, which was previously given by GALLOWAY *et al.* (2000) and SCHMIDT and BÜRGMANN (2003) through alternative DInSAR analysis. Moreover, Figures 7c and 7d show additional intriguing patterns. The former suggests that the zone with higher amplitude oscillations is close to the sharp discontinuity of the Silver Creek fault.